J. Fluid Mech. (2023), *vol*. 966, A29, doi:10.1017/jfm.2023.411

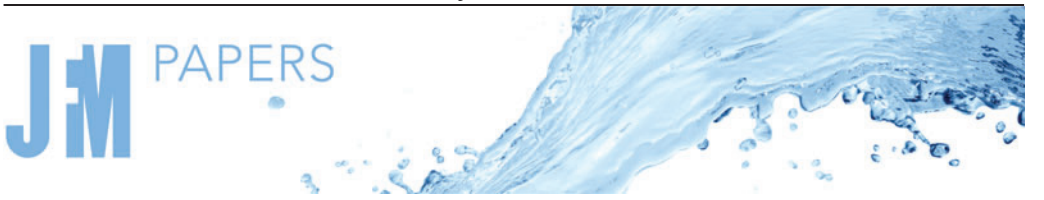

Interfacial activity dynamics of confined active droplets

Prashanth Ramesh[1,2], Babak Vajdi Hokmabad[1,3], Dmitri O. Pushkin[4], Arnold J.T.M. Mathijssen[5,†] and Corinna C. Maass[1,2,†]

[1]Max Planck Institute for Dynamics and Self-Organization, Am Faßberg 17, 37077 Göttingen, Germany

[2]Physics of Fluids Group, Max Planck Center for Complex Fluid Dynamics and J.M. Burgers Center for Fluid Dynamics, University of Twente, PO Box 217, 7500AE Enschede, Netherlands

[3]Department of Chemical and Biological Engineering, Princeton University, Princeton, NJ 08544, USA

[4]Mathematics Department, University of York, Heslington, York YO10 5DD, UK

[5]Department of Physics & Astronomy, University of Pennsylvania, 209 S 33rd St., Philadelphia, PA 19104, USA

(Received 11 January 2023; revised 11 May 2023; accepted 13 May 2023)

Active emulsions can spontaneously form self-propelled droplets or phoretic micropumps. However, it remains unclear how these active systems interact with their self-generated chemical fields, which can lead to emergent chemodynamic phenomena and multistable interfacial flows. Here, we simultaneously measure the flow and chemical concentration fields using dual-channel fluorescence microscopy for active micropumps, i.e. immobilised oil droplets that dynamically solubilise in a supramicellar aqueous surfactant solution. With increasing droplet radius, we observe (i) a migration of vortices from the posterior to the anterior, analogous to a transition from pusher- to puller-type swimmers, (ii) a bistability between dipolar and quadrupolar flows and, eventually, (iii) a transition to multipolar modes. We also investigate the long-time dynamics. Together, our observations suggest that a local build-up of chemical products leads to a saturation of the surface, which controls the propulsion mechanism. These multistable dynamics can be explained by the competing time scales of slow micellar diffusion governing the chemical buildup and faster molecular diffusion powering the underlying transport mechanism. Our results are directly relevant to phoretic micropumps, but also shed light on the interfacial activity dynamics of self-propelled droplets and other active emulsion systems.

Key words: Hele-Shaw flows, microfluidics, active matter

† Email addresses for correspondence: amaths@sas.upenn.edu, c.c.maass@utwente.nl

© The Author(s), 2023. Published by Cambridge University Press. This is an Open Access article, distributed under the terms of the Creative Commons Attribution licence (http://creativecommons.org/licenses/by/4.0), which permits unrestricted re-use, distribution and reproduction, provided the original article is properly cited.

https://doi.org/10.1017/jfm.2023.411 Published online by Cambridge University Press

1. Introduction

Phoretic mechanisms are widely used to actuate transport, be it externally mediated, e.g. by chemo- or electrophoresis, or self-generated: at macroscopic scales, phoresis can drive living organisms and culinary Marangoni cocktails (Mathijssen *et al.* 2022), and in microfluidic environments it can power self-propelled microswimmers like active colloids or droplets (Peddireddy *et al.* 2012; Herminghaus *et al.* 2014; Izri *et al.* 2014; Maass *et al.* 2016; Babu *et al.* 2022; Birrer, Cheon & Zarzar 2022; Dwivedi, Pillai & Mangal 2022; Michelin 2023), or self-driven micropumps for nutrient or fuel mixing and advection in artificial and biological systems (Gilpin, Prakash & Prakash 2017*b*; Yu *et al.* 2020; Antunes *et al.* 2022). In self-actuated systems, fluid transport is induced through non-equilibrium processes at the interface between the particle and the surrounding fluid where a slip velocity and/or tangential stresses are generated (Anderson 1989). Various phoretic mechanisms have been reported based on the type of interactions between the particle and the ambient fluid. Regardless of the type of activity, all mechanisms rely on the inhomogeneity of a surrounding field such as gradients in solute concentration (Golestanian, Liverpool & Ajdari 2005), temperature (Young, Goldstein & Block 1959) and electric fields (Bazant & Squires 2004).

In the specific case of a self-driven chemically active particle or droplet, the net motion is achieved by converting chemical free energy released by the agent into mechanical work through two distinct mechanisms: the diffusiophoretic effect, introducing a finite slip velocity at the agent interface, and the Marangoni effect, creating interfacial tangential stresses. In this context, we define activity as the conversion of undirected, chemical kinetics into mesoscopic advective flow, either driving pumping motion or a translation of the particle itself.

Reactivity gradients can be implemented by design, i.e. a built-in asymmetry, for instance by variation of the coating thickness for Janus particles (Ebbens *et al.* 2014; Campbell *et al.* 2019), in binary systems of interacting particle pairs (Reigh & Kapral 2015; Reigh *et al.* 2018) or in droplets with adsorbed colloidal caps (Ik Cheon *et al.* 2021). However, starting from a spherically isotropic particle, the only viable route to generate an interfacial reactivity gradient is by interaction with the chemical products. Chemically active droplets are among the prime model systems studied in this context. Here, an advection–diffusion instability in the chemical field around the droplet interface causes interfacial flow modes, ranging, with increasing Péclet number Pe and mode number n, from an inactive isotropic ($n = 0$) base state over a dipolar state that is propulsive in motile droplets ($n = 1$), to higher-order extensile modes, most importantly a non-propulsive quadrupolar mode for $n = 2$ (Michelin, Lauga & Bartolo 2013; Izri *et al.* 2014; Morozov & Michelin 2019). This emergence of higher interfacial modes and increasingly complex mesoscopic droplet motion with increasing Pe has been found to be quite general in experiments, irrespective of whether Pe is varied by way of chemical activity, droplet size or viscosity (Izzet *et al.* 2020; Hokmabad *et al.* 2021, 2022*b*; Suda *et al.* 2021).

It was shown in the canonical model of Michelin *et al.* (2013) and subsequent works that the most general prerequisite to set this advection–diffusion activity into motion is simply the consumption of a single chemical species at a constant rate at the interface. However, experimental realisations typically require more complicated chemical pathways. A popular model system consists of oil-in-water (alternatively, water-in-oil) emulsions in which the outer phase contains fuel supplied by a surfactant at supramicellar concentrations (Herminghaus *et al.* 2014; Izri *et al.* 2014; Izzet *et al.* 2020; Meredith *et al.* 2020; Suda *et al.* 2021). Here, the oil phase continuously solubilises by migrating from the

https://doi.org/10.1017/jfm.2023.411 Published online by Cambridge University Press

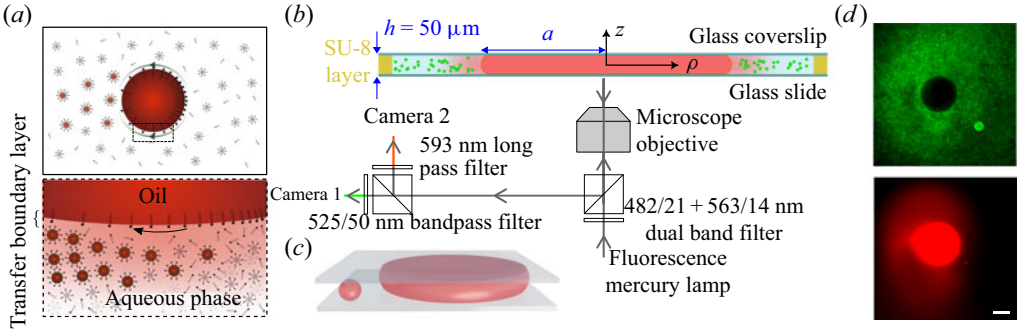

Figure 1. (*a*) Schematic of droplet propulsion mechanism and a zoomed in region around the droplet interface showing surfactant monomers, empty micelles and oil-filled micelles. (*b*) Schematic of the dual-channel microscopy set-up simultaneously visualising flow fields (camera 1) using fluorescent tracers and filled micelle concentration (camera 2) using Nile red dye in the oil droplet. (*c*) Illustration of a small, spherical self-propelling droplet vs a larger droplet immobilised by squeezing it between the glass top and bottom of the cell. (*d*) Emission from fluorescent tracers (top) and Nile red (bottom). Scale bar: 50 μm.

bulk droplet into empty or partially saturated surfactant micelles, leading to an interfacial Marangoni gradient that powers a self-supporting active interface (figure 1*a*).

Surfactant micelles and monomers constitute distinct species that diffuse at significantly different time scales, and these complex kinetics have been found to affect the details of the observed dynamics. Experimental examples include the emergence of bimodal motility through micellar accumulation at hydrodynamic stagnation points (Hokmabad *et al.* 2021), or trail avoidance stemming from chemotactic repulsion by long-lived chemical traces of other droplets (Jin, Krüger & Maass 2017; Moerman *et al.* 2017; Izzet *et al.* 2020; Lippera, Benzaquen & Michelin 2020*a*; Lippera *et al.* 2020*b*; Hokmabad *et al.* 2022*a*). Current analytical and numerical work is looking beyond the one-species approximation, e.g. considering inhibitory effects of oil-filled micelles (Morozov 2020), necessitating coupled advection–diffusion equations for species (large micelles vs monomers) with different individual diffusion time scales and *Pe*. At the current state of the art, such studies are necessarily constrained by best guesses at the currently unknown molecular dynamics like aggregation kinetics, as well as computational constraints that e.g. limit micellar aggregation numbers below typical values from the experimental literature. Thus, while we see intriguing predictions, e.g. regarding multi-stable states (coexisting different vortex patterns), there is no one-to-one comparison between theory and experiment yet. We therefore require well-controlled experimental paradigms to suggest testable geometries and provide realistic feedback to the assumptions of theory. We propose such a system in the present study on immobilised droplets, or micropumps. Here, one does not have to account for the displacements caused by the often chaotic mesoscopic motion of a motile system. Specifically, immobilisation gives access to steady state experimental conditions that allow for precise, simultaneous measurements of hydrodynamic and chemical fields.

In the experiments presented below, we measure the flow and chemical fields generated by immobilised active droplets. We then perform a hydrodynamic mode decomposition by fitting these flow structures to a version of the squirmer model in a Brinkman medium, which allows for a qualitative analysis of the interfacial flows. We explore *Pe* space via changing the droplet radius, analyse steady state and long-term time dependent flow patterns around these immobilised droplets with respect to anterior/posterior symmetry

https://doi.org/10.1017/jfm.2023.411 Published online by Cambridge University Press

and multistable states and posit hypotheses on how these patterns are shaped by the multispecies chemodynamics of the droplet solubilisation.

2. Methods

2.1. *Materials and experimental protocol*

Our experimental system consists of (S)-4-Cyano-4'-(2-methylbutyl)biphenyl (CB15, Synthon Chemicals) oil droplets immersed in an aqueous solution of the cationic surfactant tetradecyltrimethylammonium bromide (TTAB, Sigma-Aldrich). We note that, while we have used the nematogen 5CB in some of our previous studies (Krüger *et al.* 2016*a*,*b*), here we are using its branched isomer CB15 (or 5*CB) which is, while being a widely used chiral dopant, isotropic in its pure form at room temperature (Mayer *et al.* 1999). The CB15 droplets of different sizes were obtained by shaking. The TTAB surfactant concentration was fixed at 5 wt.% (critical micelle concentration, $CMC = 0.13$ wt.%). Our experimental reservoir consisted of a SU-8 photoresist spacer layer spin coated on glass, framing a rectangular cell of area 13×8 mm^2 and height of 50 μm fabricated via UV photolithography. We filled the cell with a dilute droplet emulsion and sealed it with a glass cover slip. In our analysis we included droplets with typical radii larger than 50 μm, which were compressed into flat disks of radius $a \gtrsim 60$ μm. These disks were squeezed between the top and bottom of the reservoir and exhibited only non-moving, pumping motion. This immotile state was only stable at relatively low surfactant concentrations (here, 5 wt%), and might either be caused by oil/water/glass contact line pinning, or by short range no-slip interactions in a boundary layer of surfactant and water molecules between oil and the oleophobic glass surface. The droplet shape we observed is a flat cylinder with a convex oil–water interface, as sketched in figure 1(*c*).

2.2. *Double-channel fluorescent microscopy*

To simultaneously image chemical and hydrodynamic fields, we have adapted an Olympus IX-83 microscope for dual-channel fluorescent microscopy, as shown in the light path schematic in figure 1(*b*). The fluorophores were excited using a fluorescence mercury lamp which is passed through a dual band excitation filter 482/21 + 563/14 nm. The oil phase was doped with the co-moving Nile red (Sigma-Aldrich) dye to label oil-filled filled micelles, with an emission peak of 630 nm. The tracer particles (FluoSpheres, yellow–green fluorescent, 0.5 μm in diameter), visualising the fluid flow around the droplet, emit light at a maximum of ∼510 nm. The emission was separated into two channels using a beam splitter and appropriate filters for each emission maximum, and recorded by two 4MP cameras (FLIR Grasshopper 3, GS3-U3-41C6M-C), at 24 fps for the green (tracers) and the red channel (dye) for short-time measurements. Figure 1(*d*) shows emission from fluorescent tracers (top) and Nile red (bottom). For long-time measurements, we recorded the slowly changing chemical field continuously at a reduced frame rate of 4 fps. To record tracer colloids, a higher frame rate of 24 fps was required. Due to data storage limitations, we did not record continuously for the entire experiment, but recorded 5 s sequences at 30 s intervals. Using 10× and 20× objectives focused on the cell mid-plane, the region of observation spanned 1113 μm^2 and 557 μm^2, with a focal depth of 3.06 μm and 1.10 μm, respectively. We therefore assume all extracted flow data to represent the mid-plane values in (x, y) to good accuracy.

https://doi.org/10.1017/jfm.2023.411 Published online by Cambridge University Press

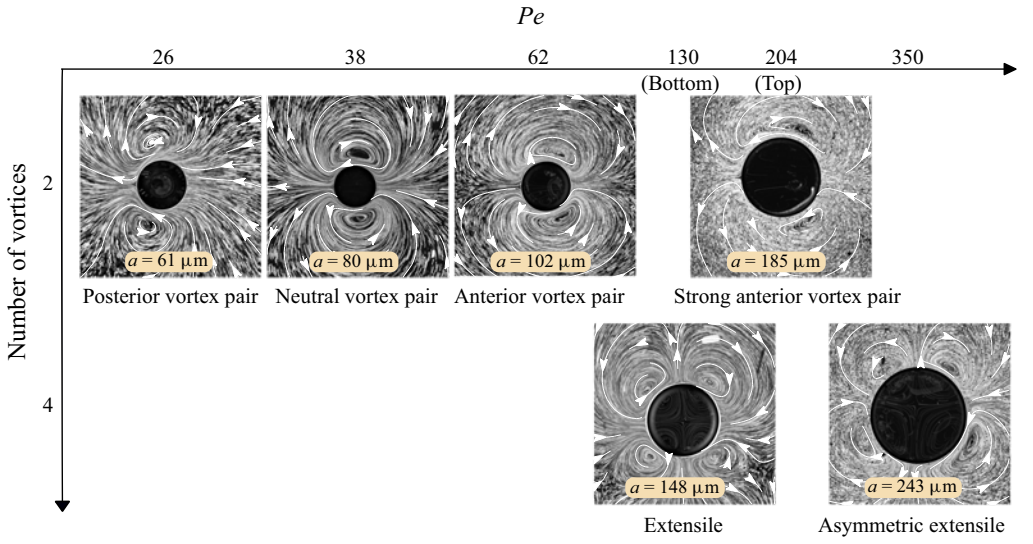

Figure 2. Streak visualisation of flow fields generated by pumping active droplets for increasing droplet radius a, with superimposed streamlines from PIV analysis. We observe a shift of the vortex pair from the droplet posterior to the anterior in the top row, corresponding to $a = 61$ μm, $a = 80$ μm and $a = 102$ μm, and on further increase of a, a bistable regime between a dipolar ($a = 185$ μm) and a quadrupolar flow mode ($a = 148$ μm). For larger radii, we only see the quadrupolar mode ($a = 243$ μm). See also supplementary material and movies S1 and S2.

2.3. *Image processing and data analysis*

We extracted the droplet position and radius a in ImageJ using the time-averaged signal from the colloidal tracer channel, where the immotile droplet appears as a dark area, A. We estimate the errors in extracted contour roundness and radius, $\Delta a/a$ to be $< 1\,\%$.

We extracted the flow field around the droplet by particle image velocimetry (PIV) of the tracer particles using the MATLAB-based PIVlab interface (Thielicke & Stamhuis 2014), with the droplet area A used as a mask. For the PIV analysis, we chose a 48×48 pixel interrogation window with 67 % overlap, at a spatial resolution of 0.28 μm px^{-1}. We then fit the two-dimensional (2-D) flow data generated by this procedure to a hydrodynamic model described below in § 2.4 within the microscope's field of view, using a least-squares fit algorithm. As PIV is unreliable near boundaries, we exclude an expanded area around the droplet, using $\rho > 1.1a$. We illustrate flow fields in figures 2 and 6, via streak images using a flowtrace algorithm (Gilpin, Prakash & Prakash 2017*a*).

For further analysis we required time-dependent chemical and tangential flow fields around the droplet perimeter $a\theta$ with the polar angle θ taken counter-clockwise from the droplet anterior (see dashed circles in figure 5*a*,*b*). The flow data were taken from PIV as close to the droplet as possible, i.e. at $\rho = 1.1a$. For the chemical field, we used the channel recording the Nile red fluorescence and extracted the intensity from an annular region around A. Since the chemical signal was oversaturated around A due to the high concentration of dye in the droplet itself, we collected fluorescence data at a distance from the interface being $\rho = 1.22a$. We separately investigated the effects of varying the droplet size on the short-time steady state flow (§ 3.1), as well as time-dependent saturation effects over long-time measurements of the order of 20 min (§ 3.4). During these long-time measurements the droplet radius reduced by approximately 7 % due to solubilisation.

https://doi.org/10.1017/jfm.2023.411 Published online by Cambridge University Press

We made sure to only include data from the first 1–2 min of experiments in the investigation of size effects shown in § 3.1.

2.4. *Flow decomposition in a 2-D Brinkman medium*

To characterise the flow in the aqueous phase, we consider a cylindrical squirmer of radius a at low Reynolds number confined between two parallel plates separated by height h. Because confinement strongly affects the flows generated by microswimmers (Mathijssen *et al.* 2016; Jeanneret, Pushkin & Polin 2019; Mondal *et al.* 2021), we follow the framework used in Jin *et al.* (2021) to evaluate the flow field $\boldsymbol{u}(x, y)$ in the mid-plane between the plates. Specifically, we approximate the 3-D Stokes equations by the 2-D Brinkman equations (Brinkman 1947; Tsay & Weinbaum 1991; Pepper *et al.* 2010; Gallaire *et al.* 2014):

$$\boldsymbol{\nabla} p = \mu(\nabla^2 - k)\boldsymbol{u}, \quad \boldsymbol{\nabla} \cdot \boldsymbol{u} = 0. \tag{2.1}$$

Here, the permeability is defined as $k = 12/h^2 = 1/\lambda^2$, in direct analogy with Darcy's law (Whitaker 1986), and λ is the slip length.

For an immotile droplet, the oil–water interface corresponds to a circle around the coordinate origin with radius $\rho = a$ in polar coordinates (ρ, θ). Assuming that this interface is impermeable, the flow field is determined by the tangential velocity. This boundary condition can be written as a harmonic expansion

$$u_\rho(\rho = a) = 0 \quad \text{and} \quad u_\theta(\rho = a) = -\frac{a}{\lambda}\sum_{n=1}^{\infty} \frac{K_{n-1}(a/\lambda)}{K_n(a/\lambda)} b_n \sin(n\theta), \tag{2.2a,b}$$

where the coefficients b_n are multiplied by a constant in terms of the Bessel functions of the second kind, K_n, to simplify the functional form of the following solution. The flow field $\boldsymbol{u}$ in the 2-D domain around the droplet, corresponding, in the Hele-Shaw cell, to the z-averaged flow in (x, y), is then given by the pumping solution (Pepper *et al.* 2010; Gallaire *et al.* 2014; Nganguia & Pak 2018)

$$u_\rho^n = b_n \left[n \left(\frac{a}{\rho}\right)^{n+1} - n \frac{a}{\rho} \frac{K_n(\rho/\lambda)}{K_n(a/\lambda)} \right] \cos(n\theta), \tag{2.3}$$

$$u_\theta{}^n = b_n \left[n \left(\frac{a}{\rho}\right)^{n+1} + \frac{a}{\lambda} \frac{K_n'(\rho/\lambda)}{K_n(a/\lambda)} \right] \sin(n\theta). \tag{2.4}$$

Henceforth, we will identify this mode decomposition of the flow as the 'Brinkman approximation'.

The flow patterns around the droplet are characterised by the first two coefficients b_1, b_2: first, their weights determine the dominant flow mode, which is dipolar for $|b_2/b_1| < 1$ and quadrupolar for $|b_2/b_1| > 1$ (Nganguia & Pak 2018; Jin *et al.* 2021). To illustrate this, supplementary material and movies are available at https://doi.org/10.1017/jfm.2023.411, where figure S1 shows the streamlines for increasing b_2/b_1 values. Second, for a primarily dipolar flow pattern, the sign of b_2 determines the location of the dominant vortex pair: $b_2 > 0$ results in an anterior and $b_2 < 0$ in a posterior location, with the droplet anterior defined at $\theta = 0$. In our fits of the experimental velocity field to this model, we use b_1, b_2 as fit parameters with $b_n = 0$ for $n > 2$ and, figure 6 excepted, all (x, y) data plots have been rotated to have the droplet's anterior or $\theta = 0$ axis pointing to the right, in positive x. We note that, using the Brinkman approximation, we assume that $u(z) \approx 0$: all monopolar

https://doi.org/10.1017/jfm.2023.411 Published online by Cambridge University Press

flow modes like a gravitational force monopole (cf. de Blois *et al.* (2019) and Hokmabad *et al.* (2022*b*) for sedimenting droplets) should be suppressed by the strong z confinement of the Hele-Shaw geometry.

3. Results

For droplets driven by micellar solubilisation, self-sustaining propulsive or pumping flows develop when the Péclet number Pe exceeds a critical threshold (Michelin *et al.* 2013); Pe is given by the ratio of advective to diffusive transport of surfactant monomers from the droplet interface to oil-filling micelles (Herminghaus *et al.* 2014), and can be estimated in the single-species picture as follows (cf. (1) and Appendix B.2 in Hokmabad *et al.* (2021), following Anderson 1989; Izri *et al.* 2014; Morozov & Michelin 2019):

$$Pe \approx \frac{18\pi^2}{k_B T} q_s r_s^2 \zeta a^2 \mu^i \left[\mu \left(\frac{2\mu + 3\zeta/a}{2\mu + 3} \right) \right]. \tag{3.1}$$

Here, a is the droplet radius, $\mu = \mu^o/\mu^i$ the viscosity ratio between the outer and inner media, $\zeta \sim 10$ nm is the characteristic length scale over which surfactant monomers interact with the droplet, $r_s \sim 10 \times 10^{-10}$ m is the length of a monomer and $q_s = D\boldsymbol{n} \cdot \nabla c$ is the isotropic interfacial surfactant desorption rate per area. We use this definition of Pe for the present geometry as well, since the underlying chemical processes are identical: qualitatively, an increase in the droplet radius a corresponds to an increase of Pe.

3.1. *Flow field characterisation and comparison with the Brinkman approximation*

We begin with a classification of the observed flow patterns around pumping flat droplets, as shown in figure 2, and the supporting supplementary material and movies S1 and S2. For small radii, $a = 61$ μm, or $Pe = 26$, we find one posterior droplet pair. With increasing droplet radius, $a = 80$ μm or $Pe = 38$, the vortex pair shifts towards the midline ('neutral' position) and finally to the droplet anterior, for $a = 102$ μm with $Pe = 62$. On further increasing the droplet radius, we observe a bistable regime, featuring either a vortex pair displaced further towards the droplet anterior ($a = 185$ μm, $Pe = 204$) or a symmetric extensile or quadrupolar flow field ($a = 148$ μm, $Pe = 130$). For even bigger droplet radii we find only the quadrupolar mode, with an increasing asymmetry in the vortex positions which shift towards the anterior ($a = 243$ μm, $Pe = 350$).

For a quantitative evaluation of the interfacial modes, we measure the flow fields by PIV and compare them with the Brinkman approximation. This decomposition gives the mode coefficients b_1, b_2 (defined in (2.2*a*,*b*)), which are shown in figure 3. Here, in the top part of panels (*a*)–(*e*) we analyse the data presented in figure 2. The streamlines show a good quantitative agreement between experimental data (top half) and the Brinkman approximation (bottom half). The mode decomposition successfully locates the vortex positions in the bulk medium, as shown by the comparison of measured and fitted streamlines in the top row; and by the small and unstructured residual flow fields in the far field (bottom row).

In analogy to the squirmer model for motile droplets (Ishikawa, Simmonds & Pedley 2006; Downton & Stark 2009), we can define a parameter $\beta = b_2/b_1$ that indicates the vortex centre position. A posterior vortex pair corresponds to $b_2/b_1 < 0$, neutral vortices to $b_2/b_1 = 0$ and anterior vortices to $b_2/b_1 > 0$. A quadrupolar configuration is caused by a dominant second mode with $|b_2/b_1| > 1$. However, for dipolar anterior vortices (figure 3*e*), the fit to the Brinkman approximation up to second

https://doi.org/10.1017/jfm.2023.411 Published online by Cambridge University Press

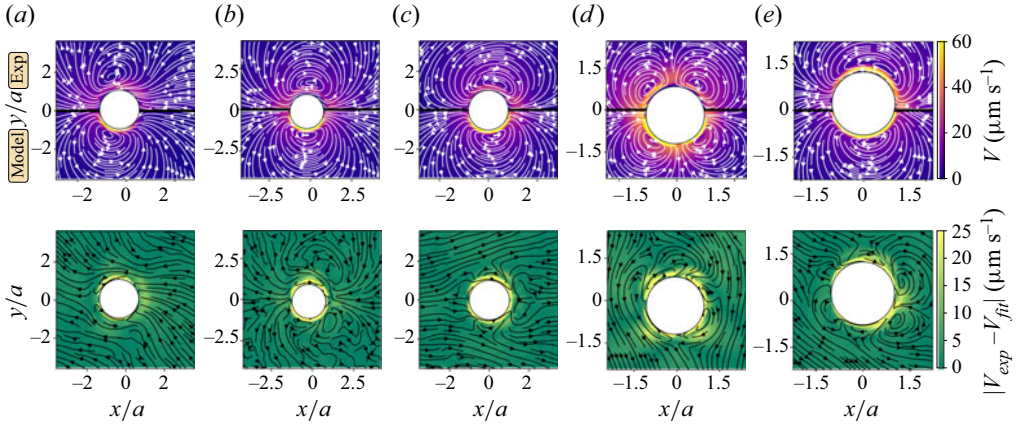

Figure 3. Top row: comparison between the experimental flow fields v_{exp} (top half of each panel) and fits to the Brinkman approximation v_{fit} (bottom half) for different Pe, with fit parameters b_1, b_2: (*a*) $Pe = 26$ ($b_2/b_1 = -0.529$), (*b*) $Pe = 38$ ($b_2/b_1 = -0.001$), (*c*) $Pe = 62$ ($b_2/b_1 = 0.191$), (*d*) $Pe = 130$ ($b_2/b_1 = 4.915$) and (*e*) $Pe = 204$ ($b_2/b_1 = 0.175$). Depending on the b_2/b_1 ratio, we note a shift of the vortex pair towards the droplet anterior, and a bistability of dipolar and quadrupolar patterns for large droplets. Bottom row: residual flow fields, $|v_{exp} - v_{fit}|$.

order somewhat under-predicts θ_v, which leads to distinct vortex structures in the residual field.

3.2. *Squirmer parameter and phase diagram*

Using the data obtained by fitting the Brinkman approximation to the experimental data, we plot the change of the squirmer parameter b_2/b_1 with the droplet radius a in figure 4(*a*). With increasing radius, b_2/b_1 increases from negative to zero and then to positive values, but still remains smaller than one, which indicates a dominant first mode. This b_2/b_1 transition reflects the vortex shift from the droplet posterior to a neutral and then an anterior position. We further evaluate the vortex angle θ_v, defined as the polar angle of the line between $\rho = 0$ and the location of $\boldsymbol{u}(x, y) = 0$ at the centre of the respective vortex (figure 4*e*). Finally, we evaluate the vortex angles in the Brinkman approximation, θ_v^{model}, and compare them with the experimentally determined values, θ_v^{exp}, vs the radius in figure 4(*b*). We observe an excellent agreement up to large radii of $a \gtrsim 150$ μm. Here, with a strong anterior shift, the experimentally determined vortex centre position is underpredicted by the Brinkman approximation.

At larger radii, we predominantly find quadrupolar flow fields, i.e. a dominant second mode. For classification, we plot the different modes in the space spanned by $|b_2/b_1|$ and a as shown in figure 4(*c*). The phase diagram is divided into three regions, namely, (*i*) 'vortex pair', (*ii*) 'bistable', featuring either a strong anterior vortex pair or a symmetric extensile flow and (*iii*) 'asymmetric extensile', where the anterior vortex pairs are displaced inwards. The dashed horizontal line, $|b_2/b_1| = 1$, separates dipolar (below) and quadrupolar (above) flow fields. For large droplets, the quadrupolar state also loses fourfold symmetry, as the vortices move towards the anterior and posterior stagnation points. To characterise this asymmetry, we plot the vortex angles for both anterior, θ_{v1}, and posterior, θ_{v2}, vortex pairs in figure 4(*d*). For the symmetric quadrupolar state, the vortex angle is $\theta_v \approx \pi/4$ (grey region), whereas in the asymmetric configuration, $\theta_v < \pi/4$ (pink region). We note

https://doi.org/10.1017/jfm.2023.411 Published online by Cambridge University Press

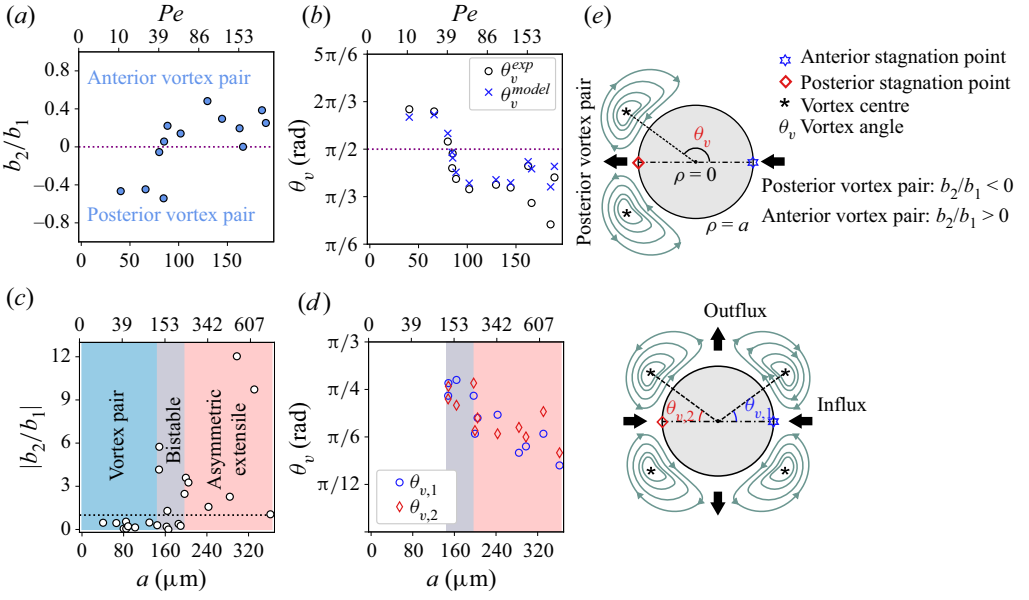

Figure 4. (*a*,*c*) Variations of squirmer parameter b_2/b_1 vs *Pe*. (*b*,*d*) Variations of angle between front stagnation point and vortex centre θ_v vs *Pe*. (*e*) Schematic defining the vortex angle.

that for both dipolar and quadrupolar asymmetric states, the vortices are pulled towards stagnation points with radial influx.

3.3. *Simultaneous chemical and flow field characterisation*

For a deeper analysis, we simultaneously measure the droplet flow fields and the chemical concentration fields using dual channel fluorescent microscopy as described above in § 2.2. Previous studies have shown that oil-filled micelles are considerably larger than the reactive species, i.e. surfactant monomers and will therefore diffuse much more slowly (Hokmabad *et al.* 2021), such that we can expect them to aggregate at stagnation points and cause secondary inhibition effects as proposed in Morozov (2020). Here, oil-filled micelles are labelled by Nile red dye co-moving with the oil phase.

In figure 5(*a–e*), we set out the relation between the chemical and flow fields for a close to neutral dipolar droplet. Panel (*a*) maps the field of the tangential velocity u_θ, with superimposed streamlines, while panel (*b*) displays a contour plot of the Nile red emission I. We further extract the profiles u_θ and $I(\theta)$ around the droplet along the dashed lines, as displayed in panels (*c*) and (*d*), with the gradient of the intensity profile in panel (*e*). If the interfacial surfactant density is depleted in the presence of filled micelles, an extremum of the gradient in the chemical field $\partial_\theta I^{max}$ correlates to a Marangoni gradient in the interface and therefore to an extremum u_θ^{max} of the tangential velocity. We have plotted the respective angles of θ_v, $\theta(u_\theta^{max})$ and $\theta(\partial_\theta I^{max})$ in panel (*f*).

As the droplet radius a increases, the vortex position shifts from the posterior at $\theta_v > \pi/2$ to the anterior at $\theta_v < \pi/2$. We observe that $\theta(u_\theta^{max})$ coincides with θ_v, and $\theta(\partial_\theta I^{max})$ shows a similar shift with increasing droplet radius, but with an offset towards higher θ values compared with θ_v and $\theta(u_\theta^{max})$. This may be due to a systematic overestimation – as noted in § 2.3, the fluorescence has to be measured away from the interface, where the micelles have already been advected further towards the droplet posterior. We propose

https://doi.org/10.1017/jfm.2023.411 Published online by Cambridge University Press

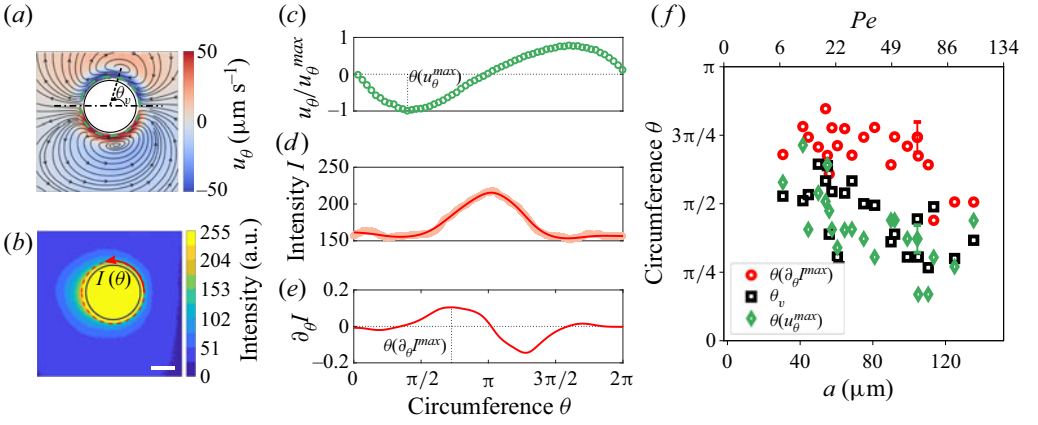

Figure 5. (*a*) Flow around a pumping droplet at $Pe = 65$, streamlines and tangential velocity u_θ (colour coded) from PIV data. Here, u_θ is extracted along the green dashed circle around the droplet interface; the black dash-dotted line marks the droplet axis. (*b*) Corresponding contour plot of discretised levels of fluorescent emission by a Nile red doped oil droplet and the filled micelles in the ambient medium. In the non-discretised raw data, the fluorescence profile around the droplet interface is extracted along the red circle to yield the profile in (*d*). Scale bar: 50 μm. (*c*) Tangential velocity profile at the interface. (*d*) Intensity profile of the filled micelle concentration around the droplet. (*e*) Intensity gradient profile corresponding to (*d*). (*f*) Variations of vortex angle θ_v (black), angle of maximum tangential velocity $\theta(u_\theta^{max})$ (green) and angle of maximum chemical gradient around the droplet $\theta(\partial_\theta I^{max})$ (red) vs *Pe*. We have added representative error bars to $\theta(u_\theta^{max})$ and $\theta(\partial_\theta I^{max})$ that estimate the systematic error from the measurement being taken at a distance from the droplet interface. All three observables decrease with increasing *Pe*.

that this displacement of $\theta(u_\theta^{max})$ and θ_v with increasing droplet radius is caused by the saturation of micelles with oil. To demonstrate saturation effects in general, we first investigate the long-term dynamics of the pumping droplet.

3.4. *Long-time evolution of the pumping droplet*

Until now, we have looked at quasi-stationary short-time dynamics. In long-term dynamics, self-interactions become more important: we expect reaction products to recirculate and interact with the droplet again after time scales longer than the advective one. This buildup of oil-filled micelles should now influence the long-term interfacial activity dynamics. To quantify this, we recorded dual-channel microvideographs of flow and chemical fields around a droplet with a dipolar flow field, and analysed the long-time interfacial dynamics (see also supplementary material and movie S3).

Figure 6(*a*) shows, for increasing time, colloidal tracer images with selected streamlines that illustrate the extracted flow field. We have plotted the tangential velocity at the interface, using the diverging colour map from panel (*c*) below, such that green corresponds to positive (counter-clockwise) and purple to negative flow, while yellow regions mark negligible flow with $|u_\theta| < 1$ μm s^{-1}, as expected for both the anterior and posterior stagnation points. At $t = 0$, the entire remaining droplet perimeter is active. With increasing time, as the droplet solubilises, oil-filled micelles build up and accumulate around the posterior stagnation point $\theta = \pm\pi$. In this area, the tangential flow speed decreases. The inactive region grows over time, as shown in the broadening yellow section of the tangential velocity map, while the vortices shift towards the anterior. At long times, $t = 22$ min, only a very small region at the droplet anterior is active and soon the entire droplet is rendered inactive.

https://doi.org/10.1017/jfm.2023.411 Published online by Cambridge University Press

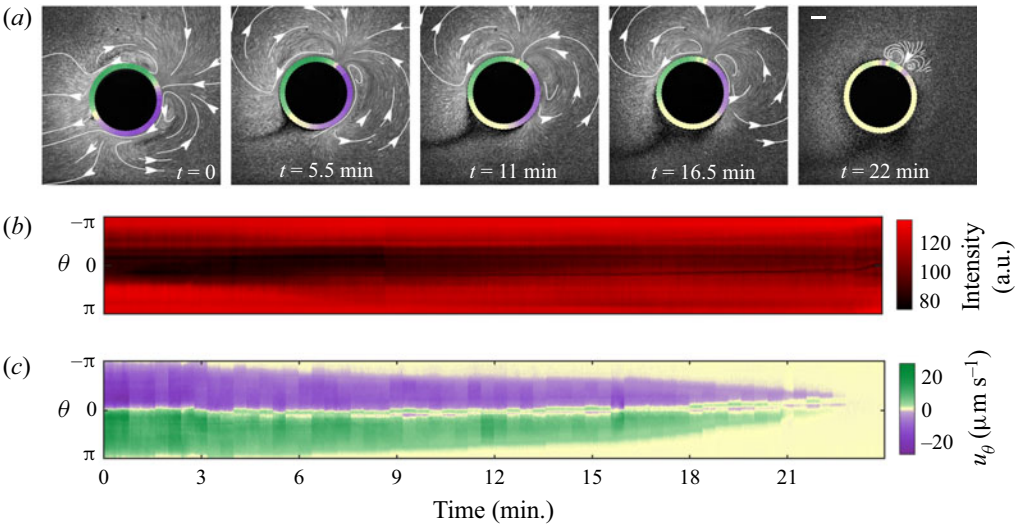

Figure 6. (*a*) Time evolution of streamlines around a pumping droplet at $Pe = 241$ and $a = 201$ μm. As time increases, the inactive region starting from the rear stagnation point grows around the interface due to saturation by filled micelles. This leads to droplet inactivity at long time. Scale bar: 100 μm. (*b*) Time evolution of filled micelle concentration around the droplet interface. Here, $\theta = 0$ indicates the anterior stagnation point. (*c*) Time evolution of the tangential velocity around the droplet interface. The colour bar also applies to the interfacial speeds plotted in (*a*). See also supplementary material and movie S3.

There is a noticeable depletion of tracer particles in the inactive region, as shown by the dark 'tail' in (*a*). This might be due to a chemo- or electrophoretic drift caused by the inhomogeneous distribution of chemical species around the posterior stagnation point (Warren, Shin & Stone 2019; Katuri *et al.* 2021), see also figure 1(*d*). If present, these flows lie below the experimental resolution of our PIV analysis and the tracer depletion is not so strong that it precludes analysis. However, over a time of 20 min, even a flow of the order of 0.1 μm s^{-1} would displace a colloid by 120 μm, which is comparable to the size of the depletion region.

To track the continuous evolution of filled micelle concentration and tangential velocity at the droplet interface, we have mapped them onto kymographs in t, θ space in figures 6(*b*) and 6(*c*). At $t = 0$, the red fluorescence from oil-filled micelles is centred around the posterior stagnation point at $\theta = \pm\pi$; the dark region around the anterior stagnation point indicates mostly empty micelles. With increasing time, as the number of oil-filled micelles increases, the red region at the posterior broadens until it fills almost the entire droplet perimeter. This is also evident from figure 6(*c*), where the green and purple bands of tangential flow corresponding to the two vortices narrow over time and recede towards $\theta = 0$, while the yellow region broadens, indicating inactivity with $|u_\theta| < 1$ μm s^{-1}. For long times, this gradual saturation renders the droplet entirely inactive. We note that, in motile droplets, one would not expect this type of saturation buildup, as they can escape their own chemical exhaust (Hokmabad *et al.* 2021).

3.5. *The effect of micelle saturation*

Finally, we want to discuss two observations. First, with increasing droplet size and Pe, we have seen a displacement trend from posterior to anterior for both the vortex-pair location, and maximum concentration gradient location. Second, long-time measurements showed

https://doi.org/10.1017/jfm.2023.411 Published online by Cambridge University Press

a saturation effect by filled micelles which leads to similar vortex location displacement, and eventually the stopping of activity. This observation is different from numerical studies on models assuming a constant interfacial activity by interaction with a single chemical species: a good example is provided in figure 3 of Morozov & Michelin (2019), where, with increasing *Pe*, the dipolar vortex centre changes from midline symmetry, to a pusher-type posterior location, to a quadrupolar state with front–back symmetry.

We note that the idealised canonical model in Michelin *et al.* (2013), Morozov & Michelin (2019) and Izri *et al.* (2014) differs from our experiments on two counts. First, it uses a spherical 3-D boundary with an axisymmetric constraint and no external forces: we are not aware of studies on a quasi-2-D geometry with a pinning force which we could use for a more direct comparison. Second, it is based on the chemodynamics of a single chemical species with a well-defined motility. It is therefore agnostic to the molecular kinetics of solubilisation, where monomers and empty or filled micelles have significantly different mobilities (Morozov 2020). We will now discuss how the differences between the evolution of vortex patterns we observe and the aforementioned numerical studies might be explained by the solubilisation kinetics alone.

Micelles will not absorb an infinite number of oil molecules (otherwise the solubilisation would create new droplets, which defies thermodynamics). Assuming, to first order, a constant flux of absorbing micelles along an active interface, and a constant rate at which they absorb oil from the boundary layer, it follows that there should be a fixed saturation time t_s, and associated length beyond which micelles will not fill any further. This length scale limits the size of the vortex patterns around the droplet, and since it is independent of the droplet size, it follows that, for a larger droplet, the vortex centre would be located closer to the droplet anterior. This is consistent with the trend we observe in the dipolar patterns in figure 2.

To extract this length scale, we analyse the steady state flow fields around droplets of different sizes (§ 3.1) with respect to two quantities. First, the length $a\theta_v$, which measures the arc length from the anterior stagnation point to the vortex centre. We assume $a\theta_v$ to scale with the saturation length, as θ_v marks the angle where the vortex streamlines begin to reorient away from the interface. Second, the average tangential velocity at the droplet interface $\bar{u}_\theta = \langle u_\theta(\rho = a, \theta)\rangle_{\theta=0.001}^{\theta=\theta_v}$. Due to the challenges of obtaining correct PIV results arbitrarily close to the interface, using the Brinkman approximation is an important tool to evaluate u_θ using the full 2-D PIV data around the droplet. The saturation time t_s defined above should now scale with $t_s = a\theta_v/\bar{u}_\theta$. We have plotted $a\theta_v$, $\bar{u}_\theta$ and t_s vs a in figure 7. We find that while both $a\theta_v$ and $\bar{u}_\theta$ increase with the droplet radius a, the saturation time $t_s = 0.92(17)$ s is constant. This indicates that for a fixed surfactant concentration the time for the micelles to become saturated is independent of the size of the droplet, and that this time scale sets the region of interfacial activity and thereby the anterior/posterior vortex configuration. This also motivates why the vortex shift with increasing *Pe* should be different from the neutral-to-pusher transition shown in Morozov & Michelin (2019), where this time scale is absent. We note that this argument does not hold for small droplets where the vortices are displaced beyond the posterior stagnation point, as a needs to be sufficiently large for the micelles to saturate while they are passing the interface.

Based on the above assumptions, we can now argue that for long times, i.e. beyond the time scale of the steady state analysed above, the continuous recirculation of filled micelles advects fewer empty micelles at the droplet anterior, which fill up faster. This leads to a gradual decrease of the saturation times and length scales, which is what we observe in figure 6 and supplementary material and movie S3.

https://doi.org/10.1017/jfm.2023.411 Published online by Cambridge University Press

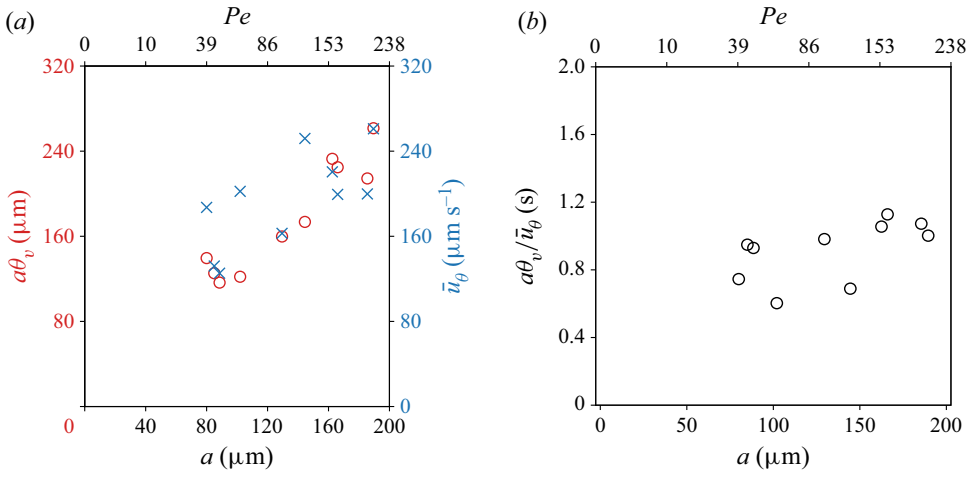

Figure 7. (*a*) Vortex arc length $a\theta_v$ and averaged tangential velocity $\bar{u}_\theta$ vs droplet radius a. (*b*) Saturation time $a\theta_v/\bar{u}_\theta$ vs droplet radius a, as extracted from the quantities plotted in (*a*).

Intuitively, this length limit might also motivate the coexistence of dipolar and quadrupolar patterns in the same *Pe* range shown in figure 2. If $\theta_v \lesssim \pi/2$, the entire posterior side of the droplet would not solubilise and become unstable towards forming a second vortex pair, as we illustrate in the top and bottom row of figure 2. Here, we note with interest a recent numerical study (Morozov 2020) which extends the canonical model to multi-species kinetics. The author assumes that slowly diffusing oil-filled micelles inhibit the adsorption of surfactant monomers onto the interface and identifies a region of Péclet numbers where indeed both dipolar and quadrupolar solutions exist simultaneously.

4. Discussion and outlook

Chemically active droplets produce the flow fields that make them self-propelling microswimmers or immotile micropumps, primarily via Marangoni gradients caused by chemical reactions at the interface. In the experiments detailed above, we have studied chemical and flow fields around immobilised droplets depending on both size and activity duration and performed a hydrodynamic mode decomposition using a Brinkman approximation to account for quasi-2-D confinement and a Péclet number *Pe* adapted to the specific chemical system. This allows us to compare our findings with recent developments in numerical and analytical models using similar *Pe* based mode stability approaches.

We confirm experimentally that the extrema in interfacial flow, and thereby the structure of the vortex field around the droplet, are correlated to gradients in the local concentration of reactivity products. Vortices and gradients shift around the perimeter with both increasing droplet size and progressing time: we have seen multistability of dipolar and quadrupolar modes, and an overall tendency of posterior-to-anterior displacement with increasing droplet size or experimental progress, which, during long-time experiments, leads eventually to an inactive droplet, where the interface is fully fouled up by chemical build-up. The analysis of our size-dependent data strongly suggests that the vortex structure is determined by the time scale of fuel conversion, as evidenced by a time-independent micellar saturation time.

Our findings provide an illustration of recent developments in analytical advection–diffusion models. Historically, minimal models assumed an uniform interfacial reaction

https://doi.org/10.1017/jfm.2023.411 Published online by Cambridge University Press

rate (Michelin *et al.* 2013; Izri *et al.* 2014), which already yields higher-order propulsive and extensile (e.g. dipolar to quadrupolar) modes with increasing *Pe* with good semi-quantitative experimental agreement. However, open questions remain for further investigation. Notably, simulations (Morozov & Michelin 2019) found a transition from neutral squirmer $\beta = 0$ to pusher, $\beta < 0$ with a posterior vortex pair, to quadrupolar extensile with increasing *Pe*, while our experiments show an increase of β with increasing *Pe*, albeit in a different geometry featuring flattened and immobilised droplets. However, in experiments on motile droplets driven by micellar solubilisation, sufficiently small swimmers are commonly found to be weak pushers as well (de Blois *et al.* 2019; Jin *et al.* 2021; Suda *et al.* 2021). Pusher-to-neutral tendencies, i.e. an increase of β, with increasing droplet radius have also been reported for moving, spherical droplets (Suda *et al.* 2021), suggesting that the divergent behaviour we found in this study is not a consequence of the different geometry, but of multi-species effects. This encourages a more in-depth investigation of the specific solubilisation kinetics in both experiment and theory.

Regarding our observation of bistable states, we note two recent studies: Bistability of dipolar and quadrupolar states was found numerically for a 3-D swimmer held stationary near a wall (Desai & Michelin 2021), thus using a single-species approach, but more complex boundary conditions than a force-free bulk. However, bistability was also found in a multi-species model of a droplet in a bulk fluid where the interfacial reactivity was assumed to be inhibited by oil-filled micelles (Morozov 2020). Interestingly, in the latter case, the region of multistability increased with the inhibition parameter.

The flow field of a Brinkman squirmer with a localised interfacial gradient, corresponding to our assumption of a predominantly inactivated interface for long times, has been evaluated as well (Gallaire *et al.* 2014), yielding very similar vortex patterns. We note, however, that these calculations were based on an preimposed interfacial tension gradient (or, experimentally, localised heating), such that the underlying physical mechanism is different from the one causing our self-evolving profile.

Beyond the implications for individual motility, multistable and higher mode flow patterns matter in the collective dynamics of active matter, and in their interactions with confined geometries. Tan *et al.* (2022) showed that developing starfish embryos generate different flow patterns during its development process, which determine their self-organisation (formation, dynamics and dissolution) into living crystals. Analogously, in artificial autophoretic systems, rotational instabilities on the individual scale (Hokmabad *et al.* 2021; Suda *et al.* 2021) can carry through to the collective dynamics, where we have recently found *Pe*-dependent stability and collective rotation in self-assembled planar clusters (Hokmabad *et al.* 2022*b*). Here, the superposition of self-generated chemical fields might well provide a mechanism for the emergence of stable collective rotational states. Our analysis of interfacial activity dynamics is also directly relevant to the study of active carpets (Mathijssen *et al.* 2018; Guzmán-Lastra, Löwen & Mathijssen 2021).

Impermeable boundaries like walls will also affect the spreading of inhibitory chemical products and affect the stability of hydrodynamic modes, as recently demonstrated for a droplet near a wall (Desai & Michelin 2021). Experimentally, such inhibitory effects in confinement can immobilise consecutive droplets in an active Bretherton scenario (de Blois *et al.* 2021) or cause reorientation up to self-trapping (Jin *et al.* 2017; Lippera *et al.* 2020*a*; Hokmabad *et al.* 2022*a*).

Understanding and modelling such phenomena from the molecular scale upwards is a daunting task, given the manifold species one has to keep track of and that the complex multistable dynamics is likely initiated by the competing time scales of slow

https://doi.org/10.1017/jfm.2023.411 Published online by Cambridge University Press

micellar diffusion governing the chemical buildup and faster molecular diffusion powering the underlying advection–diffusion mechanism. We therefore propose the tools and experimental geometry in this study as a well-defined and quantifiable testing case to investigate in matching theoretical modelling.

Supplementary material and movies. Supplementary material and movies are available at https://doi.org/10.1017/jfm.2023.411.

Acknowledgements. We gratefully acknowledge fruitful discussions with Professor J. Dunkel at MIT and experimental optics support by Dr K. Hantke at MPI-DS. We expressly acknowledge the contribution of experimental data by M. Rahalia, whom we were unable to contact at the time of submission.

Declaration of interests. The authors report no conflict of interest.

Author ORCIDs.
Prashanth Ramesh https://orcid.org/0000-0003-3264-5084;
Babak Vajdi Hokmabad https://orcid.org/0000-0001-5075-6357;
Arnold J.T.M. Mathijssen https://orcid.org/0000-0002-9577-8928;
Corinna C. Maass https://orcid.org/0000-0001-6287-4107.

References

Anderson, J.L. 1989 Colloid transport by interfacial forces. *Annu. Rev. Fluid Mech.* **21** (1969), 61–99.

Antunes, G.C., Malgaretti, P., Harting, J. & Dietrich, S. 2022 Pumping and mixing in active pores. *Phys. Rev. Lett.* **129** (18), 188003.

Babu, D., Katsonis, N., Lancia, F., Plamont, R. & Ryabchun, A. 2022 Motile behaviour of droplets in lipid systems. *Nat. Rev. Chem.* **6**, 377–388.

Bazant, M.Z. & Squires, T.M. 2004 Induced-charge electrokinetic phenomena: theory and microfluidic applications. *Phys. Rev. Lett.* **92** (6), 066101.

Birrer, S., Cheon, S.I. & Zarzar, L.D. 2022 We the droplets: a constitutional approach to active and self-propelled emulsions. *Curr. Opin. Colloid Interface Sci.* **61**, 101623.

de Blois, C., Bertin, V., Suda, S., Ichikawa, M., Reyssat, M. & Dauchot, O. 2021 Swimming droplets in 1D geometries: an active Bretherton problem. *Soft Matt.* **17**, 6646–6660.

de Blois, C., Reyssat, M., Michelin, S. & Dauchot, O. 2019 Flow field around a confined active droplet. *Phys. Rev. Fluids* **4** (5), 054001.

Brinkman, H.C. 1947 A calculation of the viscosity and the sedimentation constant for solutions of large chain molecules taking into account the hampered flow of the solvent through these molecules. *Physica* **13** (8), 447–448.

Campbell, A.I., Ebbens, S.J., Illien, P. & Golestanian, R. 2019 Experimental observation of flow fields around active Janus spheres. *Nat. Commun.* **10** (1), 3952.

Desai, N. & Michelin, S. 2021 Instability and self-propulsion of active droplets along a wall. *Phys. Rev. Fluids* **6** (11), 114103.

Downton, M.T. & Stark, H. 2009 Simulation of a model microswimmer. *J. Phys.: Condens. Matter* **21** (20), 204101.

Dwivedi, P., Pillai, D. & Mangal, R. 2022 Self-propelled swimming droplets. *Curr. Opin. Colloid Interface Sci.* **61**, 101614.

Ebbens, S., Gregory, D.A., Dunderdale, G., Howse, J.R., Ibrahim, Y., Liverpool, T.B. & Golestanian, R. 2014 Electrokinetic effects in catalytic platinum-insulator Janus swimmers. *Europhys. Lett.* **106** (5), 58003.

Gallaire, F.C., Meliga, P., Laure, P. & Baroud, C.N. 2014 Marangoni induced force on a drop in a Hele Shaw cell. *Phys. Fluids* **26** (6), 062105.

Gilpin, W., Prakash, V.N. & Prakash, M. 2017*a* Flowtrace: simple visualization of coherent structures in biological fluid flows. *J. Expl Biol.* **220** (19), 3411–3418.

Gilpin, W., Prakash, V.N. & Prakash, M. 2017*b* Vortex arrays and ciliary tangles underlie the feeding–swimming trade-off in starfish larvae. *Nat. Phys.* **13** (4), 380–386.

Golestanian, R., Liverpool, T.B. & Ajdari, A. 2005 Propulsion of a molecular machine by asymmetric distribution of reaction products. *Phys. Rev. Lett.* **94** (22), 220801.

https://doi.org/10.1017/jfm.2023.411 Published online by Cambridge University Press

GUZMÁN-LASTRA, F., LÖWEN, H. & MATHIJSSEN, A.J.T.M. 2021 Active carpets drive non-equilibrium diffusion and enhanced molecular fluxes. *Nat. Commun.* **12** (1), 1906.

HERMINGHAUS, S., MAASS, C.C., KRÜGER, C., THUTUPALLI, S., GOEHRING, L. & BAHR, C. 2014 Interfacial mechanisms in active emulsions. *Soft Matt.* **10** (36), 7008–7022.

HOKMABAD, B.V., AGUDO-CANALEJO, J., SAHA, S., GOLESTANIAN, R. & MAASS, C.C. 2022*a* Chemotactic self-caging in active emulsions. *Proc. Natl Acad. Sci. USA* **119** (24), e2122269119.

HOKMABAD, B.V., DEY, R., JALAAL, M., MOHANTY, D., ALMUKAMBETOVA, M., BALDWIN, K.A., LOHSE, D. & MAASS, C.C. 2021 Emergence of bimodal motility in active droplets. *Phys. Rev.* X **11** (1), 011043.

HOKMABAD, B.V., NISHIDE, A., RAMESH, P., KRÜGER, C. & MAASS, C.C. 2022*b* Spontaneously rotating clusters of active droplets. *Soft Matt.* **18** (14), 2731–2741.

IK CHEON, S., CAPAVERDE SILVA, L.B., KHAIR, A.S. & ZARZAR, L.D. 2021 Interfacially-adsorbed particles enhance the self-propulsion of oil droplets in aqueous surfactant. *Soft Matt.* **17**, 6742–6750.

ISHIKAWA, T., SIMMONDS, M.P. & PEDLEY, T.J. 2006 Hydrodynamic interaction of two swimming model micro-organisms. *J. Fluid Mech.* **568**, 119–160.

IZRI, Z., VAN DER LINDEN, M.N., MICHELIN, S. & DAUCHOT, O. 2014 Self-propulsion of pure water droplets by spontaneous Marangoni-stress-driven motion. *Phys. Rev. Lett.* **113** (24), 248302.

IZZET, A., MOERMAN, P.G., GROSS, P., GROENEWOLD, J., HOLLINGSWORTH, A.D., BIBETTE, J. & BRUJIC, J. 2020 Tunable persistent random walk in swimming droplets. *Phys. Rev.* X **10** (2), 021035.

JEANNERET, R., PUSHKIN, D.O. & POLIN, M. 2019 Confinement enhances the diversity of microbial flow fields. *Phys. Rev. Lett.* **123** (24), 248102.

JIN, C., CHEN, Y., MAASS, C.C. & MATHIJSSEN, A.J.T.M. 2021 Collective entrainment and confinement amplify transport by schooling microswimmers. *Phys. Rev. Lett.* **127** (8), 088006.

JIN, C., KRÜGER, C. & MAASS, C.C. 2017 Chemotaxis and autochemotaxis of self-propelling droplet swimmers. *Proc. Natl Acad. Sci. USA* **114** (20), 5089–5094.

KATURI, J., USPAL, W.E., POPESCU, M.N. & SÁNCHEZ, S. 2021 Inferring non-equilibrium interactions from tracer response near confined active Janus particles. *Sci. Adv.* **7** (18), eabd0719.

KRÜGER, C., BAHR, C., HERMINGHAUS, S. & MAASS, C.C. 2016*a* Dimensionality matters in the collective behaviour of active emulsions. *Eur. Phys. J.* E **39** (6), 64.

KRÜGER, C., KLÖS, G., BAHR, C. & MAASS, C.C. 2016*b* Curling liquid crystal microswimmers: a cascade of spontaneous symmetry breaking. *Phys. Rev. Lett.* **117** (4), 048003.

LIPPERA, K., BENZAQUEN, M. & MICHELIN, S. 2020*a* Alignment and scattering of colliding active droplets. *Soft Matt.* **17**, 365–375.

LIPPERA, K., MOROZOV, M., BENZAQUEN, M. & MICHELIN, S. 2020*b* Collisions and rebounds of chemically active droplets. *J. Fluid Mech.* **886**, A17.

MAASS, C.C., KRÜGER, C., HERMINGHAUS, S. & BAHR, C. 2016 Swimming droplets. *Annu. Rev. Condens. Matt. Phys.* **7** (1), 171–193.

MATHIJSSEN, A.J.T.M., DOOSTMOHAMMADI, A., YEOMANS, J.M. & SHENDRUK, T.N. 2016 Hydrodynamics of micro-swimmers in films. *J. Fluid Mech.* **806**, 35–70.

MATHIJSSEN, A.J.T.M., GUZMÁN-LASTRA, F., KAISER, A. & LÖWEN, H. 2018 Nutrient transport driven by microbial active carpets. *Phys. Rev. Lett.* **121** (24), 248101.

MATHIJSSEN, A.J.T.M., LISICKI, M., PRAKASH, V.N. & MOSSIGE, E.J.L. 2022 Culinary fluid mechanics and other currents in food science. arXiv:2201.12128.

MAYER, J., WITKO, W., MASSALSKA-ARODZ, M., WILLIAMS, G. & DABROWSKI, R. 1999 Polymorphism of right handed (S) 4-(2-Methylbutyl) 4′-Cyanobiphenyl. *Phase Trans.* **69** (2), 199–213.

MEREDITH, C.H., MOERMAN, P.G., GROENEWOLD, J., CHIU, Y., KEGEL, W.K., VAN BLAADEREN, A. & ZARZAR, L.D. 2020 Predator-prey interactions between droplets driven by non-reciprocal oil exchange. *Nat. Chem.* **12** (12), 1136–1142.

MICHELIN, S. 2023 Self-propulsion of chemically active droplets. *Annu. Rev. Fluid Mech.* **55** (1), 77–101.

MICHELIN, S., LAUGA, E. & BARTOLO, D. 2013 Spontaneous autophoretic motion of isotropic particles. *Phys. Fluids* **25** (6), 061701.

MOERMAN, P.G., MOYSES, H.W., VAN DER WEE, E.B., GRIER, D.G., VAN BLAADEREN, A., KEGEL, W.K., GROENEWOLD, J. & BRUJIC, J. 2017 Solute-mediated interactions between active droplets. *Phys. Rev.* E **96** (3), 032607.

MONDAL, D., PRABHUNE, A.G., RAMASWAMY, S. & SHARMA, P. 2021 Strong confinement of active microalgae leads to inversion of vortex flow and enhanced mixing. *eLife* **10**, e67663.

MOROZOV, M. 2020 Adsorption inhibition by swollen micelles may cause multistability in active droplets. *Soft Matt.* **16** (24), 5624–5632.

MOROZOV, M. & MICHELIN, S. 2019 Nonlinear dynamics of a chemically-active drop: from steady to chaotic self-propulsion. *J. Chem. Phys.* **150** (4), 044110.

https://doi.org/10.1017/jfm.2023.411 Published online by Cambridge University Press

NGANGUIA, H. & PAK, O.S. 2018 Squirming motion in a Brinkman medium. *J. Fluid Mech.* **855**, 554–573.
PEDDIREDDY, K., KUMAR, P., THUTUPALLI, S., HERMINGHAUS, S. & BAHR, C. 2012 Solubilization of thermotropic liquid crystal compounds in aqueous surfactant solutions. *Langmuir* **28** (34), 12426–12431.
PEPPER, R.E., ROPER, M., RYU, S., MATSUDAIRA, P. & STONE, H.A. 2010 Nearby boundaries create eddies near microscopic filter feeders. *J. R. Soc. Interface* **7** (46), 851–862.
REIGH, S.Y., CHUPHAL, P., THAKUR, S. & KAPRAL, R. 2018 Diffusiophoretically induced interactions between chemically active and inert particles. *Soft Matt.* **14** (29), 6043–6057.
REIGH, S.Y. & KAPRAL, R. 2015 Catalytic dimer nanomotors: continuum theory and microscopic dynamics. *Soft Matt.* **11** (16), 3149–3158.
SUDA, S., SUDA, T., OHMURA, T. & ICHIKAWA, M. 2021 Straight-to-curvilinear motion transition of a swimming droplet caused by the susceptibility to fluctuations. *Phys. Rev. Lett.* **127** (8), 088005.
TAN, T.H., MIETKE, A., LI, J., CHEN, Y., HIGINBOTHAM, H., FOSTER, P.J., GOKHALE, S., DUNKEL, J. & FAKHRI, N. 2022 Odd dynamics of living chiral crystals. *Nature* **607** (7918), 287–293.
THIELICKE, W. & STAMHUIS, E. 2014 PIVlab – towards user-friendly, affordable and accurate digital particle image velocimetry in MATLAB. *J. Open Res. Softw.* **2** (1), e30.
TSAY, R. & WEINBAUM, S. 1991 Viscous flow in a channel with periodic cross-bridging fibres: exact solutions and Brinkman approximation. *J. Fluid Mech.* **226**, 125–148.
WARREN, P.B., SHIN, S. & STONE, H.A. 2019 Diffusiophoresis in ionic surfactants: effect of micelle formation. *Soft Matt.* **15** (2), 278–288.
WHITAKER, S. 1986 Flow in porous media I: a theoretical derivation of Darcy's law. *Transp. Porous Med.* **1** (1), 3–25.
YOUNG, N.O., GOLDSTEIN, J.S. & BLOCK, M.J. 1959 The motion of bubbles in a vertical temperature gradient. *J. Fluid Mech.* **6** (3), 350–356.
YU, T., ATHANASSIADIS, A.G., POPESCU, M.N., CHIKKADI, V., GÜTH, A., SINGH, D.P., QIU, T. & FISCHER, P. 2020 Microchannels with self-pumping walls. *ACS Nano.* **14** (10), 13673–13680.

https://doi.org/10.1017/jfm.2023.411 Published online by Cambridge University Press